Electronic Supplementary Information for Local environment neighbor sensitivity analysis: visualization of cation effect at liquid-solid interface

Ryosuke Jinnouchi and Masao Suzuki Shibata

Toyota Central Research and Developments Laboratories Inc. *

(Dated: April 6, 2026)

* jryosuke@mosk.tytlabs.co.jp

S1. DETAILS OF BASIS FUNCTION ϕ_j

The descriptor $\mathbf{x}_i$ used in the MLFF method [1, 2], as implemented in VASP [3, 4], is a vector comprising two-body and three-body contributions [5].

$$\mathbf{x}_i^{\mathrm{T}} \rightarrow \left(\sqrt{\beta^{(2)}}\mathbf{x}_i^{(2)\mathrm{T}}, \sqrt{\beta^{(3)}}\mathbf{x}_i^{(3)\mathrm{T}} \right), \tag{S1}$$

Here, $\beta^{(2)}$ and $\beta^{(3)}$ $(= 1-\beta^{(2)})$ denote the weights of the two-body and three-body descriptors, $\mathbf{x}_i^{(2)}$ and $\mathbf{x}_i^{(3)}$, respectively. The vectors $\mathbf{x}_i^{(2)}$ and $\mathbf{x}_i^{(3)}$ collect the expansion coefficients of the two-body and three-body distribution functions with respect to orthonormal radial and angular basis sets [2, 5]:

$$\rho_i^{(2)}(r) = \frac{1}{\sqrt{4\pi}} \sum_{n=1}^{N_{\mathrm{R}}^0} c_{ni}\chi_{n0}(r), \tag{S2}$$

$$\rho_i^{(3)}(r,s,\theta) = \sum_{l=0}^{L_{\max}} \sum_{n=1}^{N_{\mathrm{R}}^l} \sum_{\nu=1}^{N_{\mathrm{R}}^l} \sqrt{\frac{2l+1}{2}} p_{n\nu li}\chi_{nl}(r)\chi_{\nu l}(s)P_l(\cos\theta). \tag{S3}$$

The two-body and three-body distribution functions, $\rho_i^{(2)}$ and $\rho_i^{(3)}$, are defined as follows [5]:

$$\rho_i^{(2)}(r) = \frac{1}{4\pi}\int \rho_i(r\hat{\mathbf{r}})\, d\hat{\mathbf{r}}, \tag{S4}$$

$$\rho_i^{(3)}(r,s,\theta) = \iint d\hat{\mathbf{r}}d\hat{\mathbf{s}}\ \delta(\hat{\mathbf{r}}\cdot\hat{\mathbf{s}} - \cos\theta) \left[\rho_i(r\hat{\mathbf{r}})\rho_i(s\hat{\mathbf{s}}) - \sum_{j\neq i}\rho_{ij}(r\hat{\mathbf{r}})\rho_{ij}(s\hat{\mathbf{s}}) \right], \tag{S5}$$

$$\rho_i(\mathbf{r}) = \sum_{j=1}^{N}\rho_{ij}(\mathbf{r}), \tag{S6}$$

$$\rho_{ij}(\mathbf{r}) = f_{\mathrm{cut}}\left(\left|\mathbf{r}_j - \mathbf{r}_i\right|\right) g\left(\mathbf{r} - \left(\mathbf{r}_j - \mathbf{r}_i\right)\right) \tag{S7}$$

The function g is a smoothed δ function, and f_{cut} is a cutoff function that smoothly eliminates contributions from atoms located beyond a specified cutoff radius R_{cut}. In the function $\rho_i^{(3)}$, the self-terms appearing in the power spectrum proposed by Bartók and co-workers [6, 7] are removed to ensure that the three-body distribution is represented exclusively. In this work, normalized spherical Bessel functions $\chi_{nl} = j_l(q_n r)$ and Legendre polynomials of order l are employed for χ_{nl} and P_l, respectively. Equation (3) in the main text can then be derived by defining the basis

function ϕ_j as follows:

$$\phi_j(r) = \frac{1}{\sqrt{4\pi}} c_{ji} \chi_{j0} \ \text{ for } \rho_i^{(2)}(r), \tag{S8}$$

$$\phi_j(r,s,\theta) = \sqrt{\frac{2l+1}{2}} \chi_{nl}(r)\, \chi_{\nu l}(s)\, P_l(\cos\theta) \ \text{ for } \rho_i^{(3)}(r,s,\theta), \tag{S9}$$

where the index j in Eq. (S9) denotes a set of quantum numbers n, ν, and l. The basis functions satisfy the following orthonormality conditions:

$$\int_0^\infty \phi_j(r)\phi_k(r) r^2 dr = \delta_{jk} \ \text{ for } \rho_i^{(2)}(r), \tag{S10}$$

$$\int_0^\infty \int_0^\infty \int_0^\pi \phi_j(r,s,\theta)\phi_k(r,s,\theta) r^2 dr s^2 ds \sin\theta d\theta = \delta_{jk} \ \text{ for } \rho_i^{(3)}(r,s,\theta). \tag{S11}$$

S2. DERIVATION OF EQUATION (5)

For simplicity, we introduce braket notation. Equation (3) in the main text can then be expressed as:

$$|\rho_i\rangle = \sum_j^{N_\mathrm{D}} c_{ji} |\phi_j\rangle, \tag{S12}$$

and the orthonormality conditions given in Eqs. (S10) and (S11) can be written as:

$$\langle \phi_j | \phi_k \rangle = \delta_{jk}, \tag{S13}$$

where ρ_i can be either $\rho^{(2)}$ or $\rho^{(3)}$. From the orthonormality condition given in Eq. (S12), the expansion coefficient c_{ji} can be written as:

$$c_{ji} = \langle \phi_j | \rho_i \rangle. \tag{S14}$$

A variation in ρ_i leads to a corresponding variation in c_{ji} as follows:

$$\delta c_{ji} = \langle \phi_j | \delta\rho_i \rangle. \tag{S15}$$

Since the atomic energy E_i is a function of the expansion coefficients $\{c_{ji} \mid j = 1,\ldots,N_\mathrm{D}\}$, as shown in Eq. (4) of the main text, the variation of E_i induced by a variation in ρ_i can be written as:

$$\delta E_i = \sum_{j=1}^{N_\mathrm{D}} \frac{\partial E_i}{\partial c_{ji}} \delta c_{ji} = \langle \sum_{j=1}^{N_\mathrm{D}} \frac{\partial E_i}{\partial c_{ji}} \phi_j | \delta \rho_i \rangle \,. \tag{S16}$$

By definition of the functional derivative with respect to the inner-product measure, the bracketed term is equal to $\delta E_i / \delta \rho_i$:

$$\frac{\delta E_i}{\delta \rho_i} = \sum_{j=1}^{N_\mathrm{D}} \frac{\partial E_i}{\partial c_{ji}} \phi_j . \tag{S17}$$

This equation, when combined with Eq. (4) in the main text, leads to Eq. (5) in the main text.

S3. COMPUTATIONAL WORKFLOW AND PARAMETERS FOR THE LENS ANALYSIS

The information required to compute the functional derivative $\delta E_i/\delta\rho_i$ in Eq. (5) of the main text includes the regression coefficients $\{w_{i_\mathrm{B}} \mid i_\mathrm{B} = 1,\ldots,N_\mathrm{B}\}$; the hyperparameters defining the form of the kernel basis function K and the descriptors $\mathbf{x}_i$ and $\mathbf{x}_{i_\mathrm{B}}$; the descriptor values of the local reference configurations $\{\mathbf{x}_{i_\mathrm{B}} \mid i_\mathrm{B} = 1,\ldots,N_\mathrm{B}\}$; and the descriptor values of the structures of interest, $\mathbf{x}_i$. All quantities except $\mathbf{x}_i$ in Eq. (5) in the main text are available from the VASP MLFF file, ML_FF, which is written by VASP after training. The descriptor $\mathbf{x}_i$ can be computed from the molecular dynamics (MD) trajectory of the target system, which is written to the XDATCAR file during the MD simulation. Accordingly, we developed a code that reads the required hyperparameters and regression coefficients from the ML_FF file and computes $\mathbf{x}_i$ from the trajectory stored in the XDATCAR file. The hyperparameters for the descriptors and kernel basis functions listed in Table S1 were used for the LENS analysis (see the definitions of the symbols in Refs. [2, 5, 8, 9]). For simplicity, the weight on the two-body descriptors, $\beta^{(2)}$, was set to zero, and thus, descriptors of only angular distributions $\rho_i^{(3)}$ were used. To achieve sufficient spatial resolution, the Gaussian width of the atomic distribution function g in Eq. (S7) was set to a small value of 0.16 Å, and the maximum angular momentum number L_max was set to a relatively large value of 6 in the LENS analysis. The regression coefficients were obtained by training the MLFF on the dataset described in the next section using these hyperparameters. MD trajectories were generated by 20 NVT-ensemble MD simulations at 300 K, each run for 500 ps with a time step of 0.5 fs. From the total of 10 ns of MD trajectories, 100,000 snapshots were selected. The functional derivative $\delta E_i/\delta\rho_i$ was computed from $\mathbf{x}_i$ for each snapshot using the regression coefficients and hyperparameters, and the results were averaged over all snapshots.

The numerical grids for the rotationally invariant coordinates $\mathbf{r} = (r,s,\theta)$ were set to 100 points in each range from 0 to the cutoff radius, $R_\mathrm{cut}^{(3)}$, for r and s, and from 0 to π for θ. Prior to applying LENS, we performed a numerical test to verify whether the analytical functional derivative given by Eq. (5) in the main text agrees with the numerical derivative obtained using a finite-difference method. In this test, one snapshot was selected from the MD trajectory, and the functional derivative $\delta E_i/\delta\rho_i$ was computed using Eq. (5) in the main text. Next, an expansion coefficient $c_{ji} = p_{nvli}$ was displaced by a small value of $\pm\varepsilon(=\pm 0.003)$, and the corresponding distribution functions $\rho_i^\pm$ and local energies $E_i^\pm$ were calculated using Eq. (S3) and Eq. (4) in the main text, respectively. Here, $A^\pm$ denotes the quantity A evaluated with the small displacement $\pm\varepsilon$

applied to the expansion coefficient. We then examined whether the following relation is satisfied:

$$E_i^+ - E_i^- = \int_0^\infty \int_0^\infty \int_0^\pi \frac{\delta E_i}{\delta \rho_i} \left[\rho_i^+(r,s,\theta) - \rho_i^-(r,s,\theta)\right] r^2 s^2 \sin\theta \, dr ds d\theta. \tag{S18}$$

The numerical test indicated that the equation was satisfied within a relative error of 0.05 %. Consequently, the formulation and numerical settings accurately reproduce the functional derivative.

The calculations were performed on 16 cores of Intel Xeon Platinum 6548N (2.8 GHz). The measured wall time was approximately 15,700 s for the LENS analysis of 100,000 snapshots, which is negligible compared with the computational cost of the training and production runs required to compute the free-energy changes explained in the next section. The computational bottleneck lies in the evaluation of the expansion coefficients $c_{ji} = p_{nvli}$ in Eq. (S3), whose cost scales linearly with the number of atoms, indicating that the method is applicable to large systems.

Table S 1. Parameter sets of the descriptors and kernel basis functions used in the LENS analysis. The units of $R_{\mathrm{cut}}^{(3)}$ and $\sigma_{\mathrm{atom}}^{(3)}$ are Å.

ζ	4	$\beta^{(3)}$	1.0	$R_{\mathrm{cut}}^{(3)}$	5.0	$\sigma_{\mathrm{atom}}^{(3)}$	0.16	$N_{\mathrm{R}}^{(3)}$	24	$L_{\mathrm{max}}^{(3)}$	6

S4. THERMODYNAMIC INTEGRATION

Here, we describe the MLFF-aided FP-TI approach. The reaction free energy ΔA^{ML} is calculated by integrating the derivative of Hamiltonian $\left\langle \partial H^{\mathrm{ML}}/\partial\lambda \right\rangle_{\lambda}$ along a coupling path λ from the reactant state at $\lambda = 0$ to the product state at $\lambda = 1$ using MLFFs:

$$\Delta A^{\mathrm{ML}} = \int_0^1 \left\langle \frac{\partial H^{\mathrm{ML}}}{\partial\lambda} \right\rangle_{\lambda} d\lambda. \tag{S19}$$

The symbol H^{ML} denotes the Hamiltonian in which the potential energy is evaluated as $\lambda E_1^{\mathrm{ML}} + (1-\lambda)E_0^{\mathrm{ML}}$, where E_0^{ML} and E_1^{ML} are the MLFF-calculated potential energies of the reactant and product states, respectively. The residual error of the MLFFs caused by incompleteness in short range interactions and lack of long-range interactions is then accurately corrected by an additional TI performed from the MLFF potential energy surface to that obtained from the FP method, as follows:

$$\Delta A_{\lambda}^{\mathrm{FP-ML}} = \int_0^1 \left\langle \frac{\partial H_{\lambda}^{\mathrm{FP-ML}}}{\partial\eta} \right\rangle d\eta. \tag{S20}$$

The symbol $H_{\lambda}^{\text{FP-ML}}$ denotes the Hamiltonian in which the potential energy is evaluated as $\eta E_{\lambda}^{\mathrm{FP}} + (1-\eta)E_{\lambda}^{\mathrm{ML}}$, where $E_{\lambda}^{\mathrm{FP}}$ denotes the FP potential energy for the reactant ($\lambda = 0$) and product ($\lambda = 1$) states. The FP reaction free energy ΔA^{FP} is obtained as $\Delta A^{\mathrm{ML}} + \Delta A_1^{\text{FP-ML}} - \Delta A_0^{\text{FP-ML}}$.

In practical calculations, the computational standard hydrogen electrode (CSHE) method [10] is employed, whereby ΔA is approximated using a linear approximation [11] as $\Delta A_{\mathrm{OH}} + eU$, with e denoting the elementary charge, U the electrode potential referenced to the standard hydrogen electrode (SHE), and ΔA_{OH} the reaction free energy of the reduction reaction OH$*$ + 1/2 H_2 $\rightarrow$ H_2O. The quantity ΔA_{OH} can be decomposed into the sum of two contributions: the reaction free energy ΔA_1 associated with bond formation between the adsorbed OH$*$ species and a hydrogen atom at the solid-liquid interface, OH$*$ + H $\rightarrow$ H_2O, and the reaction free energy ΔA_2 corresponding to the dissociation of an H_2 molecule, 1/2 H_2 $\rightarrow$ H [12, 13]:

$$\Delta A_{\mathrm{OH}} = \Delta A_1 + \Delta A_2. \tag{S21}$$

ΔA_2 is evaluated using a simple ideal-gas model, whereas ΔA_1 is obtained via MLFF-aided TI, car-

ried out from a noninteracting hydrogen atom and a solid-liquid interface containing OH$*$ without H to the fully interacting hydrogen atom, which covalently bonds with OH$*$ to form H_2O at the interface. From ΔA_{OH}, the redox potential U_{OH} of the reaction, OH$*$ + H^+ + e^- $\rightarrow$ $*$ + H_2O, is calculated as:

$$U_{\mathrm{OH}} = -\frac{A_{\mathrm{OH}}}{e}. \tag{S22}$$

This approach enables a precise evaluation of the reaction free energy, referenced to the free energy of a well-defined ideal gas of H_2, by explicitly accounting for anharmonic fluctuations of interfacial molecules at finite temperature through MD calculations.

For light hydrogen atoms, nuclear quantum effects contribute to the free energy difference. These effects were incorporated using the harmonic correction employed in previous studies [12, 14]. The parameters and computational settings are identical to those used in our previous publication; see Ref. [12] for details.

S5. INTERFACIAL MODELS

The interfaces between water and pristine Pt(111) surfaces in the presence of an alkaline cation X^+ (X = Li, K, or Cs) and a homogeneously distributed positive background charge are modeled as shown in Fig. S1. As explained in the main text and in our previous work [12], this study adopts the method introduced by Nørskov and co-workers [10] to calculate the redox potential of OH formation. This approach assumes that the effect of interfacial electric fields is small and evaluates redox potentials using electrically neutral interfacial models, based on a first-order approximation with respect to the interfacial excess charge [11]. Accordingly, the solid surfaces are approximated by four-layer slabs with a $3\times2\sqrt{3}$ surface periodicity.

One OH adsorbate per unit cell was placed on one side of the slab, corresponding to an OH coverage of 1/12 ML, and one hydrogen atom was introduced during the TI using the MLFF to generate an additional water molecule at the interface.

The interfacial model was constructed as follows. The lattice parameter of Pt was set to 4.03 Å, based on bulk pure Pt calculated using the FP method [15]. A water layer containing one alkaline cation was inserted into the vacuum gap between the slabs. To prepare the initial configurations of water and the cation, a 1 ns classical MD simulation of bulk liquid water was performed using the polymer consistent force field (PCFF) [16]. The equilibrated solution layer was then placed between the slabs. The number of water molecules was set to 47 and 48 for the Pt slabs with and without the OH adsorbate, respectively. After further relaxation of the interfacial structures by 100 steps of structural optimization using the FP method, active-learning MD simulations were carried out to generate the MLFFs. Once the MLFFs were constructed, the unit-cell length along the direction perpendicular to the surface was equilibrated using a 100 ps NP_zT ensemble MD simulation with the generated MLFFs. The cell length was then adjusted to the equilibrated value, and production runs were performed using these structures as the initial configurations.

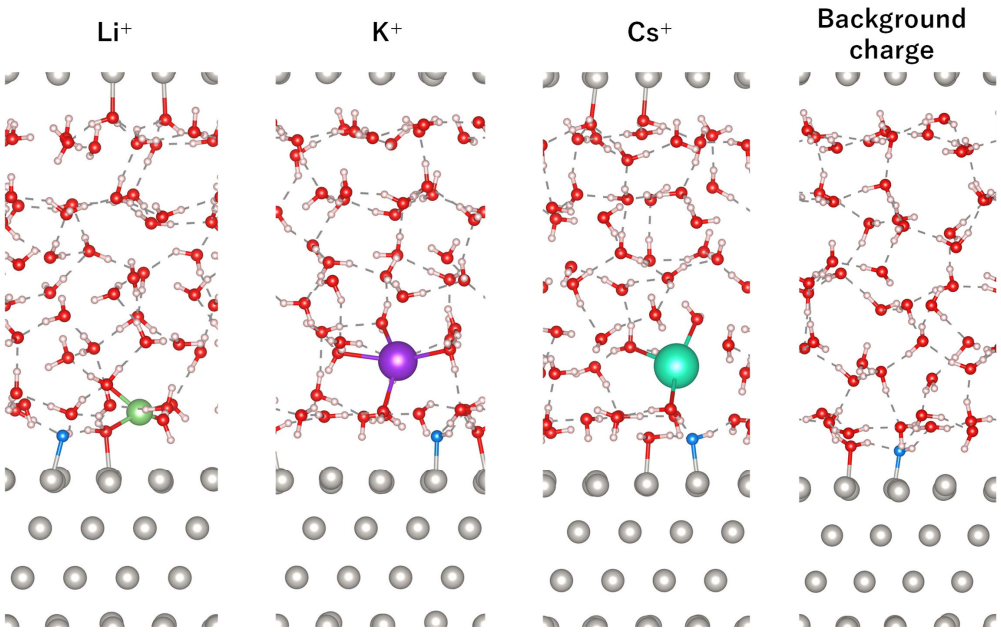

Figure S 1. Interfacial models used in the MD calculations and LENS analyses.

S6. TRAINING OF MLFFS AND THEIR ACCURACY

The MLFFs were trained following the same protocol as that used in our previous study [12]. The reference points $\{\mathbf{x}_{i_\mathrm{B}} \mid i_\mathrm{B} = 1, \ldots, N_\mathrm{B}\}$ and the structures providing training data for energies, forces, and stress-tensor components were collected on the fly during active-learning MD simulations implemented in VASP [1–4]. The hyperparameters used for the MLFFs in the MD calculations are summarized in Table S2. The Bayesian framework enables accurate predictions of energies, forces, and their associated uncertainties, thereby allowing efficient on-the-fly sampling of reference structures during MD simulations of the target systems. A single MLFF was trained for each surface system described in Section S5. For both the reactant and product states, a 100 ps heating simulation from 300 to 500 K followed by a 100 ps cooling simulation from 500 to 300 K was performed. For uncertainty estimation, the spilling factor proposed by Miwa and Ohno [17] was employed, with the threshold set to 0.005. By the end of the cooling simulations, the MLFFs ceased collecting structures and reference points, indicating that they had sufficiently learned the information required for the simulations.

The numbers of collected structures (N_st) and reference points (N_B) for each MLFF are listed in Table S3. Consistent with previous studies [1, 2, 5, 8, 12, 18–23], N_st ranges from 180 to 308. Scatter plots comparing energies, forces, and stress-tensor components predicted by the MLFFs with those obtained from FP calculations are shown in Fig. S2. The same figure also presents the root mean square errors (RMSEs) of the MLFFs for test structures that appear during the TI from the MLFFs to the FP potential energy surface. The generated MLFFs achieve RMSEs of 1.6-3.8 meV atom^{-1} for energies, 0.052-0.063 eV Å^{-1} for forces, and 0.96-1.62 kbar for stress-tensor components, which are comparable to values reported in previous studies [1, 2, 5, 8, 13, 18–23].

In all FP calculations, exchange-correlation (XC) interactions between electrons were treated using the RPBE+D3 functional [24–26]. As shown in Table S4, the RPBE functional reproduces the experimental adsorption energies of O, OH, and CO on the Pt(111) surface in vacuum [27–30] more accurately than the state-of-the-art XC functional such as r^{2}SCAN [31]. For CO, RPBE has also been shown to best reproduce results obtained from the random phase approximation (RPA), an accurate beyond-DFT method [32]. We therefore employed RPBE augmented with the D3 dispersion correction, which is known to provide a reasonable description of the structural and diffusional properties of liquid water [33, 34]. It should be noted that RPBE+D3 slightly overestimates these adsorption energies and yields values close to those obtained with the r^{2}SCAN

functional. The plane-wave cutoff energy was set to 520 eV, and Brillouin-zone integrations were performed using a $3\times3\times1$ **k**-point mesh. The projector-augmented-wave (PAW) atomic reference configurations were $1s^1$ for H, $1s^2 2s^1$ for Li, $2s^2 2p^4$ for O, $3s^2 3p^6 4s^1$ for K, $5s^2 5p^6 6s^1$ for Cs, and $5d^9 6s^1$ for Pt [35].

Table S 2. Parameter sets of the descriptors and kernel basis functions for the MLFFs used in the MD calculations. The units of $R_{\mathrm{cut}}^{(2)}$, $R_{\mathrm{cut}}^{(3)}$, $\sigma_{\mathrm{atom}}^{(2)}$ and $\sigma_{\mathrm{atom}}^{(3)}$ are Å.

ζ	4	$\beta^{(2)}$	0.5	$R_{\mathrm{cut}}^{(2)}$	6.0	$\sigma_{\mathrm{atom}}^{(2)}$	0.5	$N_{\mathrm{R}}^{(2)}$	8		
		$\beta^{(3)}$	0.5	$R_{\mathrm{cut}}^{(3)}$	4.0	$\sigma_{\mathrm{atom}}^{(3)}$	0.5	$N_{\mathrm{R}}^{(3)}$	6	$L_{\mathrm{max}}^{(3)}$	2

Table S 3. The number of structures N_{st} calculated using the FP method to generate the training data and the number of kernel basis functions N_{B} for the MLFFs.

Cation type X^+	N_{st}	N_{B} (H)	N_{B} (O)	N_{B} (Pt)	N_{B} (X)
Li^+	264	19395	8151	2294	263
K^+	180	15579	6955	1845	180
Cs^+	308	21048	8708	2841	290
Background charge	260	6250	2405	707	

Table S 4. Adsorption energies of O, OH, and CO on the Pt(111) surface in vacuum calculated using four representative exchangecorrelation (XC) functionals and compared with experimental values. Energies are given in eV.

XC functional	O	OH	CO
PBE	4.24	2.19	1.69
RPBE	3.79	1.92	1.42
RPBE+D3	3.90	2.17	1.82
R^2SCAN	4.08	2.11	1.80
Exp.	3.48[a]	1.5-2.5[b]	1.37[c]

[a] Experimental data taken from Ref. [27].

[b] Experimental results and estimations taken from Ref. [28, 29].

[c] Experimental data taken from Ref. [30].

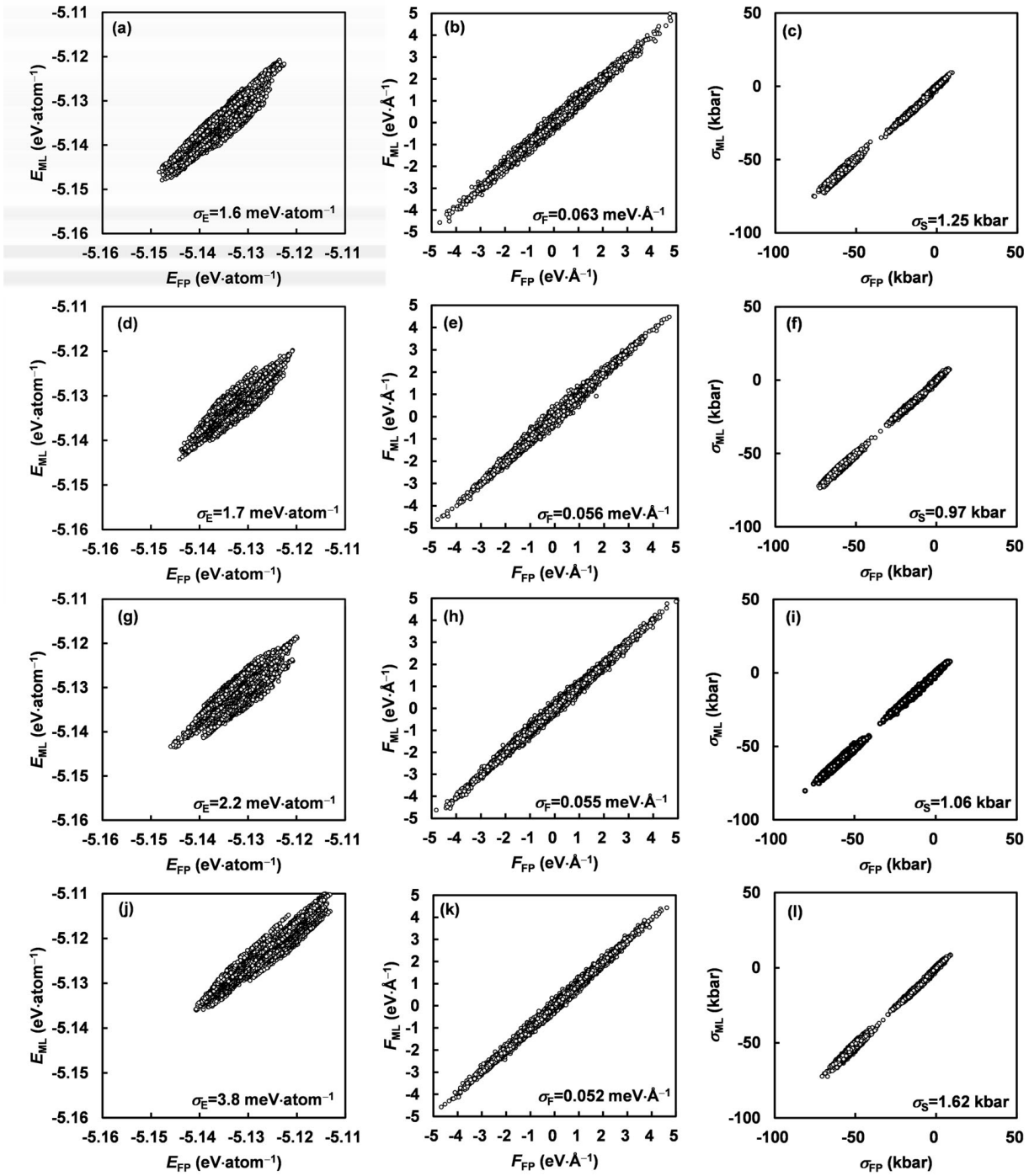

Figure S 2. Energies, forces, and stress-tensor components predicted by the MLFFs versus those calculated using the FP method for 15,000 test data points from the X^++48H_2O/Pt(111) system and 15,000 test data points from the X^++OH+47H_2O/Pt(111) system (X = Li, K, Cs, and background charge), taken from the TI calculations from the MLFF to the FP potential energy surface. The symbols σ_E, σ_F, and σ_S denote the root mean square errors for the energy, force, and stress-tensor data, respectively.

S7. COMPUTATIONS OF INTERFACIAL DIFFUSION COEFFICIENT D_{int}

The diffusion coefficient D_{int} of the alkaline cations Li^+, K^+, and Cs^+ along the direction parallel to the Pt(111) surface was calculated from the slope of the mean square displacement (MSD) of each cation. A total of twenty 500 ps NVT-ensemble MD simulations, starting from different initial positions and velocities, were performed, and the resulting diffusion coefficients were averaged. Figure S3 shows the averaged MSDs. In all MD simulations, the cations remained localized at the interface, indicating that the computed diffusion coefficients reasonably represent interfacial diffusion.

Figure S4 shows the correlation between the computed redox potential U_{OH} and the interfacial diffusion coefficient D_{int}. Smaller cations are more strongly trapped by $OH*$ through attractive interactions. Consequently, both D_{int} and U_{OH} decrease with decreasing ionic radius.

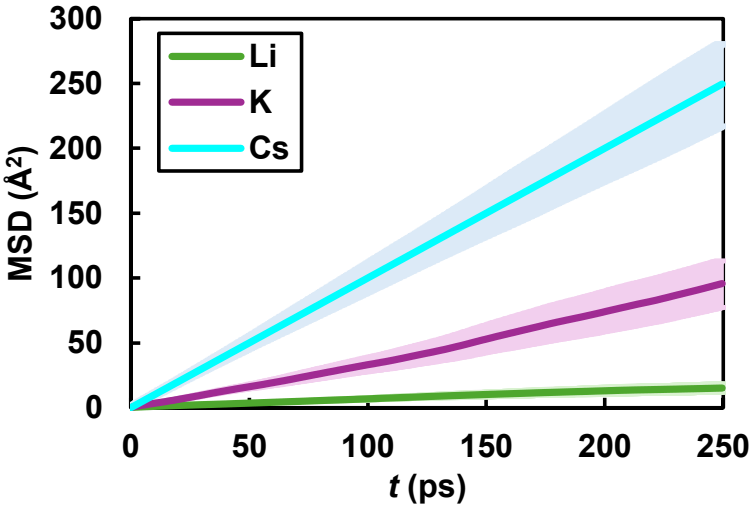

Figure S 3. Mean square displacements (MSDs) of alkali ions along the direction parallel to the Pt surface. The shaded regions indicate the error bars, evaluated as the standard deviation divided by the square root of the sample size (20).

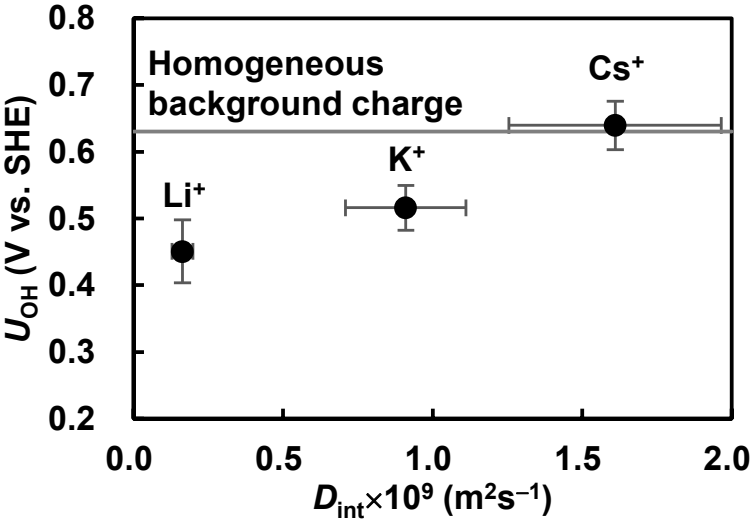

Figure S 4. Computed redox potential U_{OH} versus the computed interfacial diffusion coefficient D_{int} of the cations. The horizontal line indicates the result obtained with the diffusive uniform homogeneous background charge.

S8. BADER CHARGE AND ELECTRONIC STRUCTURE ANALYSES

Bader charge analysis shows that OH$*$ and the alkali cations in all three interfacial systems stably carry charges of $-0.5e$ and $+0.9e$, respectively, throughout the MD simulations, as shown in the insets of Fig. 1 in the main text. The partial density of states (PDOS) analysis indicates that the majority of the *s*-states of the alkali cations lie about 2 eV above the Fermi level, as shown in Fig. S5. These charge and electronic structure analyses clearly indicate that all cations have lost electrons and are in a state close to $+1e$. Accordingly, the interactions between the cations and OH$*$ are mainly electrostatic. These interactions are neither covalent, arising from the occupation of hybridized bonding orbitals, nor due to polarization. Although all ions carry nearly identical monopole charges, their sizes differ. The smaller Li^+ cation can approach OH$*$ more closely, resulting in stronger electrostatic interactions than for the other ions. The role of the Pt surface is not merely that of a spectator; by stabilizing a negatively charged OH$*$ species through metaladsorbate hybridization, it indirectly enables electrostatic coupling with the cation.

Bader charge analysis [36] was performed on 100 interfacial structures randomly selected from the 10 ps NVT-ensemble FPMD trajectories generated in the second TI step described in Section S4. The parameters for the FP calculations were set to be the same as those described in Section S6. The Bader charges of OH$*$ and the alkali cations, averaged over these 100 configurations and shown in Fig. 1 of the main text, indicate that OH$*$ carries a negative charge of approximately $-0.5e$, while the alkali cations retain positive charges close to $+0.9e$ regardless of the cation species, where e denotes the elementary charge. The standard deviations of the charges across the 100 samples were small, with values of $0.02e$ for OH$*$ and $0.005e$ for the cations. PDOS analyses were executed on 10 snapshots taken from the MD trajectories.

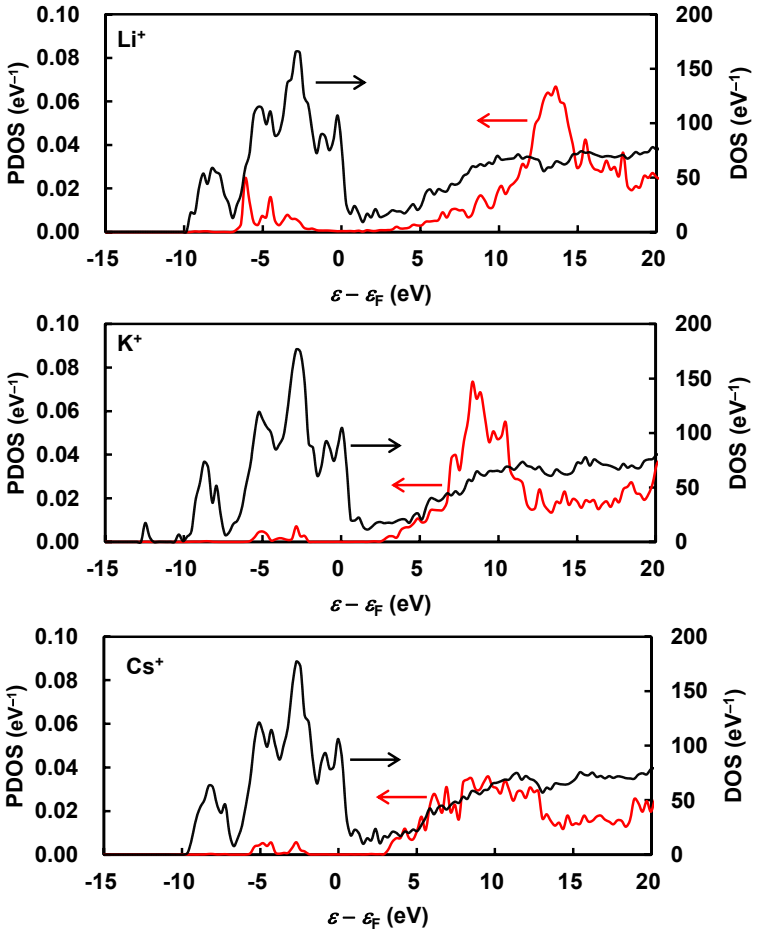

Figure S 5. Total (black) and partial (red) densities of states for the *s*-orbital of alkali cations in interfacial systems.

S9. THREE-BODY DISTRIBUTIONS

Figure S6 shows the three-body probability distribution $\rho_i^{(3)}(r,s,\theta)$, which represents the probability density of finding an H atom at a distance r to $r+dr$ from this O atom and a cation X^+ (X = Li, K, or Cs) at a distance s to $s+ds$ from the same O atom, with $\angle$HOX = θ = 110°, as illustrated in the insets. The absolute value of $\rho_i^{(3)}$ for Li^+ is orders of magnitude larger than those for K^+ and Cs^+ because Li^+ is sharply localized much closer to the O atom than the larger cations.

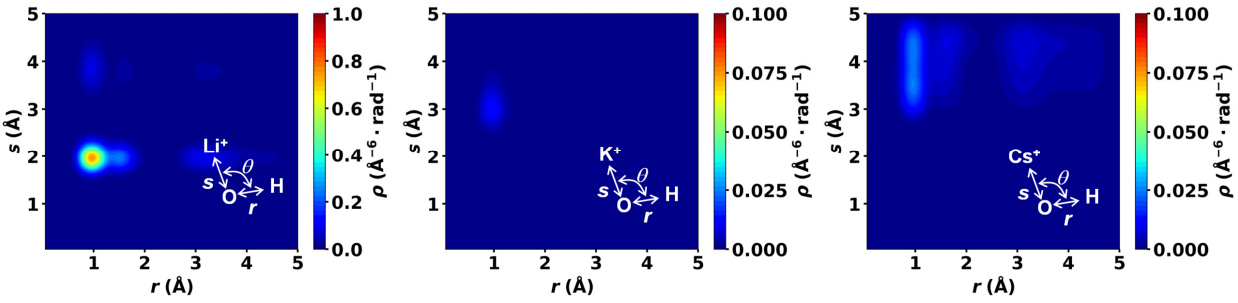

Figure S 6. The three-body probability distribution $\rho_i^{(3)}(r,s,\theta)$ of finding an H atom at a distance r to $r+dr$ from this O atom and a cation X^+ (X = Li, K, or Cs) at a distance s to $s+ds$ from the same O atom, with $\angle$HOX = θ = 110°, as illustrated in the insets.

[1] Ryosuke Jinnouchi, Jonathan Lahnsteiner, Ferenc Karsai, Georg Kresse, and Menno Bokdam. Phase transitions of hybrid perovskites simulated by machine-learning force fields trained on the fly with bayesian inference. *Phys. Rev. Lett.*, 122:225701, Jun 2019.

[2] Ryosuke Jinnouchi, Ferenc Karsai, and Georg Kresse. On-the-fly machine learning force field generation: Application to melting points. *Phys. Rev. B*, 100:014105, 2019.

[3] G. Kresse and J. Furthmüller. Efficient iterative schemes for ab initio total-energy calculations using a plane-wave basis set. *Phys. Rev. B*, 54:11169–11186, Oct 1996.

[4] G. Kresse and J. Furthmüller. Efficiency of ab-initio total energy calculations for metals and semiconductors using a plane-wave basis set. *Computational Materials Science*, 6(1):15–50, 1996.

[5] Ryosuke Jinnouchi, Ferenc Karsai, Carla Verdi, Ryoji Asahi, and Georg Kresse. Descriptors representing two- and three-body atomic distributions and their effects on the accuracy of machine-learned inter-atomic potentials. *The Journal of Chemical Physics*, 152(23):234102, 2020.

[6] Albert P. Bartók, Mike C. Payne, Risi Kondor, and Gábor Csányi. Gaussian approximation potentials: The accuracy of quantum mechanics, without the electrons. *Phys. Rev. Lett.*, 104:136403, 2010.

[7] Albert P. Bartók, Risi Kondor, and Gábor Csányi. On representing chemical environments. *Phys. Rev. B*, 87:184115, May 2013.

[8] Ryosuke Jinnouchi, Ferenc Karsai, and Georg Kresse. Machine learning-aided first-principles calculations of redox potentials. *npj Computational Materials*, 10(1):107, May 2024.

[9] Ryosuke Jinnouchi, Ferenc Karsai, and Georg Kresse. Absolute standard hydrogen electrode potential and redox potentials of atoms and molecules: Machine learning aided first principles calculations. *Chem. Sci.*, 16:2335–2343, 2025.

[10] J. K. Nørskov, J. Rossmeisl, A. Logadottir, L. Lindqvist, J. R. Kitchin, T. Bligaard, and H. Jónsson. Origin of the overpotential for oxygen reduction at a fuel-cell cathode. *The Journal of Physical Chemistry B*, 108(46):17886–17892, Nov 2004.

[11] Ryosuke Jinnouchi. Grand-canonical first principles-based calculations of electrochemical reactions. *Journal of The Electrochemical Society*, 171(9):096502, sep 2024.

[12] Ryosuke Jinnouchi and Saori Minami. The melamine-driven solvation effect promotes oxygen reduction on a platinum catalyst: Machine learning-aided free energy calculations. *The Journal of Physical Chemistry Letters*, 16(1):265–273, Jan 2025.

[13] Ryosuke Jinnouchi and Saori Minami. Machine learning force fields in electrochemistry: From fundamentals to applications. *ACS Nano*, 19(25):22600–22644, Jul 2025.

[14] Jun Cheng, Marialore Sulpizi, and Michiel Sprik. Redox potentials and pKa for benzoquinone from density functional theory based molecular dynamics. *The Journal of Chemical Physics*, 131(15):154504, 10 2009.

[15] Ryosuke Jinnouchi, Kensaku Kodama, Tatsuya Hatanaka, and Yu Morimoto. First principles based mean field model for oxygen reduction reaction. *Phys. Chem. Chem. Phys.*, 13:21070–21083, 2011.

[16] H. Sun. Force field for computation of conformational energies, structures, and vibrational frequencies of aromatic polyesters. *Journal of Computational Chemistry*, 15(7):752–768, 1994.

[17] Kazutoshi Miwa and Hiroshi Ohno. Molecular dynamics study on β-phase vanadium monohydride with machine learning potential. *Phys. Rev. B*, 94:184109, Nov 2016.

[18] Ryosuke Jinnouchi, Ferenc Karsai, and Georg Kresse. Making free-energy calculations routine: Combining first principles with machine learning. *Phys. Rev. B*, 101:060201, Feb 2020.

[19] Ryosuke Jinnouchi, Kazutoshi Miwa, Ferenc Karsai, Georg Kresse, and Ryoji Asahi. On-the-fly active learning of interatomic potentials for large-scale atomistic simulations. *The Journal of Physical Chemistry Letters*, 11(17):6946–6955, Sep 2020.

[20] Ryosuke Jinnouchi, Ferenc Karsai, Carla Verdi, and Georg Kresse. First-principles hydration free energies of oxygenated species at waterplatinum interfaces. *The Journal of Chemical Physics*, 154(9):094107, 03 2021.

[21] Ryosuke Jinnouchi. Molecular dynamics simulations of proton conducting media containing phosphoric acid. *Phys. Chem. Chem. Phys.*, 24:15522–15531, 2022.

[22] Ryosuke Jinnouchi, Saori Minami, Ferenc Karsai, Carla Verdi, and Georg Kresse. Proton transport in perfluorinated ionomer simulated by machine-learned interatomic potential. *The Journal of Physical Chemistry Letters*, 14(14):3581–3588, Apr 2023.

[23] Saori Minami and Ryosuke Jinnouchi. Accelerating anhydrous proton conduction via anion rotation and hydrogen bond recombination: a machine-learning molecular dynamics. *J. Mater. Chem. A*, 11:16104–16114, 2023.

[24] B. Hammer, L. B. Hansen, and J. K. Nørskov. Improved adsorption energetics within density-functional theory using revised perdew-burke-ernzerhof functionals. *Phys. Rev. B*, 59:7413–7421, Mar 1999.

[25] Stefan Grimme, Jens Antony, Stephan Ehrlich, and Helge Krieg. A consistent and accurate ab initio parametrization of density functional dispersion correction (DFT − D) for the 94 elements H-Pu. *The Journal of Chemical Physics*, 132(15):154104, 2010.

[26] Stefan Grimme. Density functional theory with london dispersion corrections. *WIREs Computational Molecular Science*, 1(2):211–228, 2011.

[27] Y. Y. Yeo, L. Vattuone, and D. A. King. Calorimetric heats for co and oxygen adsorption and for the catalytic co oxidation reaction on pt{111}. *The Journal of Chemical Physics*, 106(1):392–401, 01 1997.

[28] Charles E. Mooney, Louis C. Anderson, and Jack H. Lunsford. Energetics for the desorption of hydroxyl radicals from a platinum surface. *The Journal of Physical Chemistry*, 97(11):2505–2506, Mar 1993.

[29] T. J. Schmidt, P. N. Ross, and N. M. Markovic. Temperature-dependent surface electrochemistry on pt single crystals in alkaline electrolyte: part 1: co oxidation. *The Journal of Physical Chemistry B*, 105(48):12082–12086, Dec 2001.

[30] F. Abild-Pedersen and M.P. Andersson. Co adsorption energies on metals with correction for high coordination adsorption sites a density functional study. *Surface Science*, 601(7):1747–1753, 2007.

[31] James W. Furness, Aaron D. Kaplan, Jinliang Ning, John P. Perdew, and Jianwei Sun. Accurate and numerically efficient r2scan meta-generalized gradient approximation. *The Journal of Physical Chemistry Letters*, 11(19):8208–8215, Oct 2020.

[32] L. Schimka, J. Harl, A. Stroppa, A. Grüneis, M. Marsman, F. Mittendorfer, and G. Kresse. Accurate surface and adsorption energies from many-body perturbation theory. *Nature Materials*, 9(9):741–744, Sep 2010.

[33] Tobias Morawietz, Andreas Singraber, Christoph Dellago, and Jörg Behler. How van der waals interactions determine the unique properties of water. *Proceedings of the National Academy of Sciences*, 113(30):8368–8373, 2016.

[34] Pablo Montero de Hijes, Christoph Dellago, Ryosuke Jinnouchi, and Georg Kresse. Density isobar of water and melting temperature of ice: Assessing common density functionals. *The Journal of Chemical Physics*, 161(13):131102, 10 2024.

[35] G. Kresse and D. Joubert. From ultrasoft pseudopotentials to the projector augmented-wave method. *Phys. Rev. B*, 59:1758–1775, Jan 1999.

[36] W Tang, E Sanville, and G Henkelman. A grid-based bader analysis algorithm without lattice bias. *Journal of Physics: Condensed Matter*, 21(8):084204, jan 2009.